ACS Catalysis

Research Article

pubs.acs.org/acscatalysis

Selective Catalytic Oxidation of H_2S over Well-Mixed Oxides Derived from $Mg_2Al_xV_{1-x}$ Layered Double Hydroxides

Xin Zhang,[†] Zhuo Wang,[†] Nanli Qiao,[†] Siqiu Qu,[‡] and Zhengping Hao[†,*]

[†]Department of Environmental Nanomaterials, Research Center for Eco-Environmental Sciences, Chinese Academy of Sciences, Beijing 100085, People's Republic of China

[‡]Center of Research & Development, Shandong Sunway Petrochemical Engineering Share Co., Ltd, Beijing 100015, People's Republic of China

Supporting Information

ABSTRACT: A series of $Mg_2Al_xV_{1-x}$–LDH (LDH = layered double hydroxide) was synthesized by using a facile method, and well-mixed derived oxides were obtained after calcinations. These catalysts were further tested for H_2S selective oxidation. Meanwhile, the physicochemical properties of the catalysts were investigated by various methods. It was observed that vanadium species existed mainly in the form of isolated V^{5+} in distorted $[VO_4]$,$Mg_3V_2O_8$ and VO^{2+}. Significantly, these catalysts exhibited high catalytic activities in a relatively lower range of reaction temperatures (100–200 °C) as a result of the well-dispersed vanadium species and excellent moderate basicity property. A catalytic reaction mechanism was proposed as follows: H_2S was first adsorbed on the Mg–O–Mg band of MgO (moderate basic sites), forming S^{2-} and H_2O, then the S^{2-} was oxidized to S_n by V^{5+}, simultaneously, forming oxygen vacancies and V^{4+}. Finally, V^{4+} was oxidized to V^{5+} by O_2, and O^{2-} was incorporated into oxygen vacancies. In addition, the catalyst deactivation was mainly due to the decrease in moderate basic sites. Moreover, the formed less-active $VOSO_4$ also contributed to the catalyst deactivation.

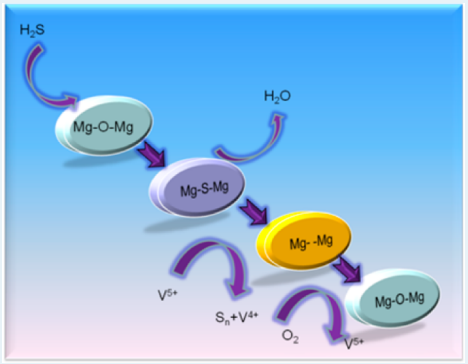

KEYWORDS: *layered double hydroxides, derived oxides, H_2S selective oxidation, catalytic activity, catalytic mechanism*

1. INTRODUCTION

Because the environmental regulations concerning the release of sulfur-containing gas have become more stringent, H_2S contained in acidic gases needs to be carefully treated prior to emission to the atmosphere. Nowadays, the most well-known technique is the Claus process;[1] however, almost 1% H_2S is left in Claus tail gas because of the thermodynamic limitations.[2−4] Fortunately, various additional purification processes have been used, such as absorption, adsorption, and selective catalytic oxidation technique.[5] Among them, the selective catalytic oxidation technique has been of great research interest in recent decades because it can directly catalytically oxidize H_2S to elemental sulfur. The irreversible reaction equations are as follows (eq 1 as the main reaction, eqs 2 and 3 as side reactions):[6]

$$H_2S + (1/2)O_2 \rightarrow (1/n)S_n + H_2O \quad (1)$$

$$(1/n)\,S_n + O_2 \rightarrow SO_2 \quad (2)$$

$$H_2S + (3/2)O_2 \rightarrow SO_2 + H_2O \quad (3)$$

In the reaction, SO_2 could be formed via the deep oxidation of H_2S or the further oxidation of elemental sulfur, causing a decrease in sulfur yield. Therefore, the sulfur yield strongly depends on the catalyst selectivity.

Vanadium oxides are active for H_2S selective oxidation, and many vanadium oxides supported catalysts, such as V_2O_5 supported on pillared clay[5,7] and mesoporous materials,[8] have been investigated as a kind of potential catalysts for H_2S selective oxidation. All of them present good catalytic activities in the temperature range of 200–300 °C.[9] As is known, the catalytic activity of the supported catalysts depends mainly on the highly dispersed active phase.[10] However, the particle size and macrodistribution (uniform, egg shell, egg yolk, or egg white)[11] of the active phase cannot be controlled easily. Meanwhile, the large particle can block the pore. In addition, the choice of an optimal support is absolutely a complicated problem[12] because the support can react with H_2S or products to form sulfate, which causes a decrease in the catalytic activities or even the destruction of the catalyst. Furthermore, the relatively higher reaction temperature for H_2S selective oxidation is not beneficial to energy-saving. Herein, the above problems should be considered seriously to further apply the catalyst in industrial emission control. Thus, it is desirable to modify vanadium species to obtain a catalyst with high catalytic performance at a relatively lower temperature.

Received: December 10, 2013
Revised: March 29, 2014
Published: April 1, 2014

   dx.doi.org/10.1021/cs500303y | ACS Catal. 2014, 4, 1500−1510

Layered double hydroxides (LDHs), also known as hydrotalcite-like compounds, are anionic clay materials.[13] The chemical composition of LDHs can be expressed by the general formula $[M^{II}_{1-x}M^{III}_{x}(OH)_2]^{x+}[A_{x/n}{}^{n-}\cdot yH_2O]^{x-}$,[14] wherein M^{II} and M^{III} are divalent and trivalent metal cations,[15] A^{n-} is an n-valent anion, and x usually has values between 0.25 and 0.33. In particular, in recent years, LDHs and their derivatives have been intensively investigated as catalysts and catalyst supports in many aspects because the acid/base properties can be easily tuned[16] and their composition can be varied,[15] which leaves vast flexibility for the better selection of various cations in these materials for H_2S selective oxidation. The corresponding composite oxides can be obtained after calcinations, wherein the vanadium species can be well-dispersed and incorporated into the catalyst steadily. Thus, layered double hydroxides are considered as a kind of attractive and suitable material to disperse and modify vanadium species.

$Mg_2Al_xV_{1-x}$–LDH can be synthesized by partially replacing Al^{3+} through the Rives method;[17] however, the preparation process was particularly tedious and complicated. In the present work, a facile method was provided to obtain $Mg_2Al_xV_{1-x}$–LDH. As expected, the catalytic activity can be enhanced due to the outstanding acidic/base properties and reasonable thermal stability. Moreover, the physicochemical properties of catalysts were characterized by various measurements. In addition, the catalytic and catalyst deactivation mechanisms for H_2S selective oxidation over these catalysts were explored. To the best of our knowledge, it is the first time that $Mg_2Al_xV_{1-x}$–LDH-derived oxides have been used and studied for H_2S selective oxidation.

2. EXPERIMENTAL SECTION

2.1. Catalyst Preparation. The synthesis of $Mg_2Al_xV_{1-x}$–LDH was carried out using a modified version of Xu's method.[18] $MgCl_2$, $AlCl_3{\cdot}6H_2O$, NaOH, and VCl_3 were used as starting materials. In a typical synthesis process, 60 mmol of $MgCl_2$, x mmol of $AlCl_3$, and $(20-x)$ mmol of VCl_3 ($Mg^{2+}/(Al^{3+} + V^{3+}) = 2$, $V^{3+}/(Al^{3+} + V^{3+}) = 0.1, 0.3, 0.5, 0.7, 1$) were dissolved in 200 mL of decarbonated water previously purged by nitrogen. Then the solution was quickly (within 5s) added into 800 mL of NaOH solution (0.15 M) under vigorous stirring, followed by 15 min of stirring in a nitrogen atmosphere. $Mg_2Al_xV_{1-x}$–LDH was obtained after centrifuging the mixture three times and drying overnight at 40 °C. Finally, the derived oxide catalysts were obtained by calcining the LDH materials at 550 °C for 4 h. These catalysts were denoted as $Mg_2Al_xV_{1-x}O$.

2.2. Characterization of the Catalysts. X-ray diffraction (XRD) patterns were recorded on a PANalytical X'Pert PRO powder diffraction system using Cu K radiation(λ = 0.154 18 nm) in the 2θ range of 10–80° (scanning rate of 0.5°/min).

UV–vis diffuse reflectance spectra (UV–vis DRS) were recorded in air against $BaSO_4$ in the region of 12 500–24 000 cm^{-1} on a Hitachi UV-3000 spectrometer.

Energy dispersive spectrograph (EDS) was performed on an IXRF system for composition analysis of the synthesized catalysts.

Thermal stability was investigated with thermogravimetry (TG, Seteram, Labsys). Typically, around 30 mg of sample was heated in an Al_2O_3 crucible at a constant heating rate of 10 °C/min from 25 to 1000 °C, with air purging at a flow rate of 30 mL/min.

X-ray photoelectron spectra (XPS) were recorded with a Thermo Electron Escalab250 instrument using Al Ka radiation. The base pressure was 5×10^{-8} Pa. The binding energies were calibrated using the C 1s peak of contaminant carbon (BE = 285 eV) as the standard and quoted with a precision of ±0.2 eV.

BET surface areas and textural properties of catalysts were determined by nitrogen adsorption–desorption isotherms using a gas sorption analyzer NOVA1200. Prior to N_2 adsorption measurement, the samples were degassed at 300 °C for 3h.

The electron paramagnetic resonance (EPR) spectra were recorded on a JES FA200 spectrometer at room temperature.

DRIFTS-MS spectra of H_2S adsorption on these catalysts were collected on the BrukerTensor 27 spectrometer in the range of 600–4000 cm^{-1} after 256 scans at a resolution of 4 cm^{-1}. A 0.5 g portion of catalyst was placed in the IR flow cell and treated at 300 °C in a He flow for 0.5 h after calcination in air at 550 °C for 4 h. Next, the cell was cooled to 100 °C, and the background spectrum was taken. The value was subtracted from the sample spectrum obtained at 100 °C. Then, a gas mixture (5000 ppm of H_2S in He, 200 mL/min) was passed through the catalyst bed for 20 min. After that, the FTIR spectrum was recorded, then the cell was cooled to room temperature and the used catalysts were replaced with fresh ones. The above operation was repeated, and FTIR spectra were recorded at the other designed temperatures (140, 160, 180 °C). In all cases, the effluent stream was analyzed online using a quadruple mass spectrometer (Omnistar Thermostar).

H_2 temperature-programmed reduction (H_2-TPR) experiments were conducted on a Micromeritics Chemisorb 2720 apparatus. TPR profiles were obtained by passing a 5% H_2/He flow (50 mL/min) through the pretreated catalyst (about 100 mg). The temperature was increased from room temperature to 900 °C at a rate of 10 °C/min. Hydrogen concentration in the effluent was continuously monitored by a thermo conductivity detector. Prior to each TPR run, the catalyst was preheated in a He flow from room temperature to 300 °C and held for 30 min.

CO_2 temperature-programmed desorption (CO_2-TPD) was carried out on the same apparatus as that in H_2-TPR. In the process, the sample was heated from room temperature to 900 °C at a rate of 10 °C/min in pure He. Before each TPD test, a 100 mg sample was preheated in a He flow from room temperature to 300 °C and held for 30 min. After cooling to room temperature, 20% CO_2/He was fed to the reactor at 50 mL/min for 30 min, then pure He was fed to the reactor at 50 mL/min for 30 min to purge away any residual CO_2.

2.3. Catalytic Performance Tests. All tests were performed in a continuous flow fixed-bed quartz reactor at atmospheric pressure. A 0.5 mL catalyst (20–40 mesh) was placed in the central section of the reactor. The mixture gas containing 5000 ppm of H_2S, 2500 ppm of O_2 and the balance gas (N_2) were fed into the reactor at 200 mL/min of the total gas flow rate (GHSV = 24000 h^{-1}) and reacted in the temperature range of 100–200 °C. After reaction, the effluent stream was detected by a gas chromatograph (GC126) equipped with a FPD and TCD. A condenser was located at the bottom of the reactor to trap the sulfur gas in the effluent stream. Instantaneous fractional conversion of H_2S, sulfur selectivity, and sulfur yield were defined as

$$H_2S\ \text{conversion} = \frac{(H_2S)_{in} - (H_2S)_{out}}{(H_2S)_{in}}$$

dx.doi.org/10.1021/cs500303y | ACS Catal. 2014, 4, 1500–1510

$$\text{sulfur selectivity} = \frac{(H_2S)_{in} - (H_2S)_{out} - (SO_2)_{out}}{(H_2S)_{in} - (H_2S)_{out}}$$

$$\text{sulfur yield} = (H_2S \text{ conversion}) \times (\text{sulfur selectivity})$$

3. RESULTS AND DISCUSSION

3.1. Transformation of Hydrotalcites to Derived Oxides. XRD analysis is used to clarify the structure of the synthesized LDH. The XRD patterns of all samples are presented in Figure 1A. The peaks that appeared at 10.7°, 22.4°, 34.6°, 39.2°, 45.5°, and 60.6° are related to the (003), (006), (009), (015), (018), and (110) planes, which are the typical diffractions of LDH materials.[19] In addition, the (003), (006), and (009) planes indicate the formation of crystalline layered structures with rhombohedral symmetry (3R), although the (015) and (018) planes are characteristic of polytype $3R_1$ hydrotalcites. Furthermore, according to the value of lattice parameter a (calculated on the basis of d(110)) of pure $Mg(OH)_2$ (a = 0.315) and Al-rich LDH (a = 0.304),[20] if the metal ions were not dispersed well in the hydroxide layers, the peak corresponding to the (110) plane should be overlapped and broad. Therefore, the sharp peak of the (110) plane reveals quite a good dispersion of metal ions in the hydroxide layers.[21] Nevertheless, the diffraction intensity of all planes becomes gradually lower with the rise of vanadium content, which is in accordance with the previous reports.[22−25] As is known, the diffraction intensity of the planes is contributed by the brucite-like layer and anion interlayer; however, the LDH materials in this study have the same anion layer. Thus, the lower diffraction intensity gradually observed results from the higher atomic scattering factor with the rise of vanadium content.[26,27] Hence, it indicates that vanadium species are successfully incorporated into LDH brucite-like layer.

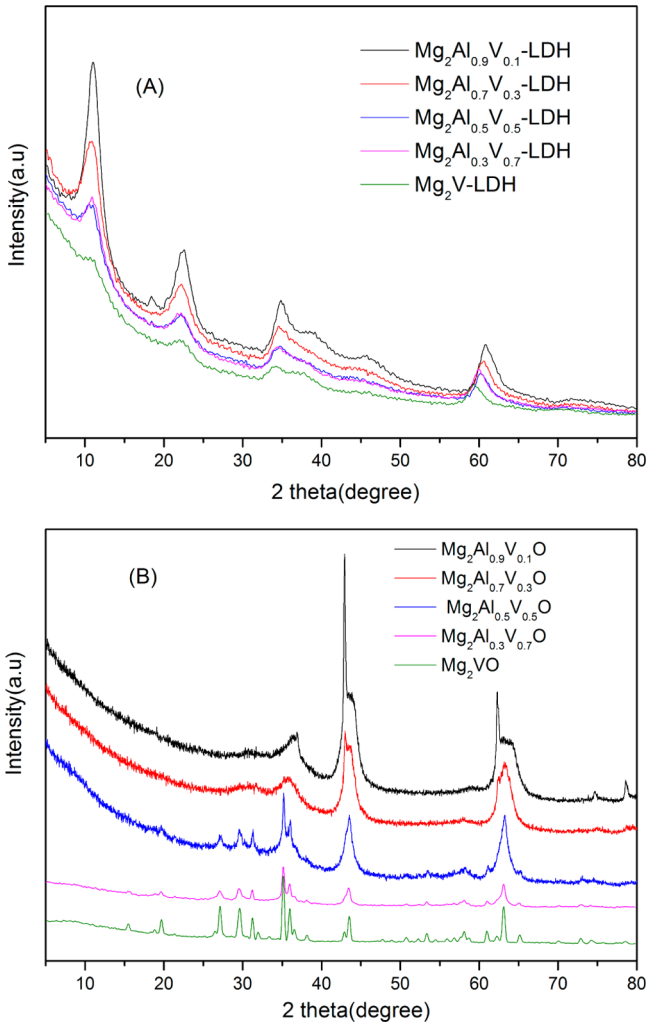

Figure 1. XRD patterns of (A) $Mg_2Al_xV_{1-x}$−LDH and (B) $Mg_2Al_xV_{1-x}O$ catalysts.

The lattice parameters are calculated on the basis of $d_{(110)}$ for parameter a and $d_{(003)}$, $d_{(006)}$ for parameter c, respectively. Parameter a links to the cation−cation distance in the brucite-like layer, and parameter c corresponds to the total thickness of the brucite-like layer and the interlayer distance.[28,29] The detailed information on calculated parameters a and c are collected in Table 1. Parameter a increases with the rise of the vanadium content. This can be explained by the fact that the ionic radius of V^{3+} (0.64 Å) is larger than Al^{3+} (0.53 Å).[30] Thus, it also indicates that V^{3+} has replaced the Al^{3+} in the brucite-like layers. Moreover, the decrease in parameter c with the increase of the vanadium content can be attributed to the modified electrostatic interactions between the brucite-like layer and the interlayer when another metal is introduced into the LDH layer structure.[31] In addition, the decrease in $d_{(003)}$ suggests some distortion of the LDH layer structure induced by the partial replacement of Al^{3+} by V^{3+}.

Table 1. Chemical Composition and Lattice Parameters of Parent Samples

sample	$V^{3+}/(V^{3+}+Al^{3+})^a$ (molar)	$d_{(003)}$ spacing (Å)	lattice parameters	
			a	c
$Mg_2Al_{0.9}V_{0.1}$−LDH	0.12	8.30	3.04	24.49
$Mg_2Al_{0.7}V_{0.3}$−LDH	0.32	8.16	3.05	24.24
$Mg_2Al_{0.5}V_{0.5}$−LDH	0.51	8.10	3.06	24.17
$Mg_2Al_{0.3}V_{0.7}$−LDH	0.67	8.05	3.08	24.15
Mg_2V−LDH	1	7.96	3.1	23.88

$^a V^{3+}/(V^{3+} + Al^{3+})$ are analyzed by EDS

The XRD patterns of the derived oxides (Figure 1B) show the complete transformation from the hydrotalcite to the oxide phase. It is obvious that the gradual replacement of Al by V in the hydrotalcite structure leads to the gradual changes in the phase composition. In the case of $Mg_2Al_{0.9}V_{0.1}O$ and $Mg_2Al_{0.7}V_{0.3}O$ catalysts, similar characteristics are obtained. The patterns are dominated by the peaks at 36.9°, 43.4° and 63.4°, which can be ascribed to the diffractions by planes (111), (200), and (220) of the periclase (MgO) structure;[32−34] however, the peaks shift toward relatively higher angles compared with pure MgO, implying the partial existence of Al^{3+} in the MgO lattice. Simultaneously, the sharp peaks appearing at 42.8° and 62.1° demonstrate the existence of magnesium orthovanadate ($Mg_3V_2O_8$), whose intensity decreases with an increase in the vanadium content to 0.3 (which means $V^{3+}/(Al^{3+}+V^{3+})$ = 0.3). It indicates that the $Mg_2Al_{0.9}V_{0.1}O$ catalyst contains more $Mg_3V_2O_8$ than the

dx.doi.org/10.1021/cs500303y | ACS Catal. 2014, 4, 1500−1510

catalyst $Mg_2Al_{0.7}V_{0.3}O$. Moreover, other peaks corresponding to $Mg_3V_2O_8$ appeared in the range of 25°−35° when the vanadium content rose to 0.5 and 0.7, and the $Mg_3V_2O_8$ content increased with an additional vanadium content increase from 0.5 to 0.7. In general, the peaks attributed to Al-doped MgO predominate the pattern for the $Mg_2Al_{0.5}V_{0.5}O$ catalyst; likewise, $Mg_3V_2O_8$ for the $Mg_2Al_{0.3}V_{0.7}O$ catalyst. Moreover, the main diffraction feature belongs almost to the contribution of the Mg orthovanadate phase ($Mg_3V_2O_8$) when the vanadium content increases to 1. In addition, the surface morphologies of all catalysts were also examined by SEM (Supporting Information Figure.S1). It can be noted significantly that the morphologies were similar when the vanadium content was in the range of 0.1−0.7, whereas larger particles were formed and rather different features were observed when the vanadium content rose to 1. It implies changes in the catalyst composition, which is in good agreement with the XRD results.

The thermal behaviors of the LDH materials during heating in air are illustrated in Figure 2. Three well differentiated

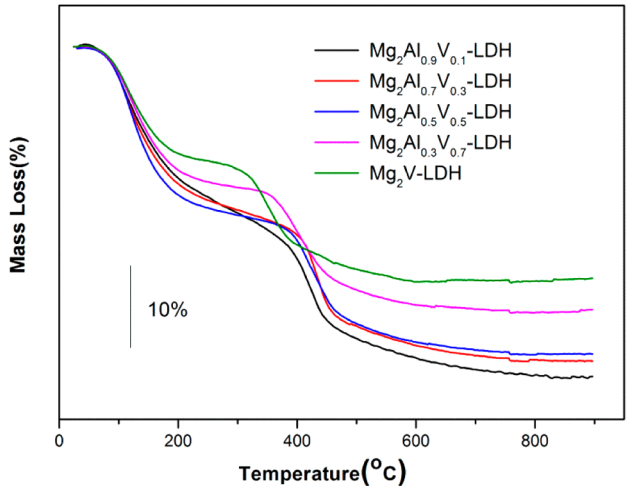

Figure 2. TG patterns of $Mg_2Al_xV_{1-x}$−LDH.

weight-loss steps, which are the typical characteristics of LDH materials, are recorded in all cases.[35] The first step occurred at 100−300 °C and can be attributed to the removal of interlayer water molecules.[36] The second step occurred at 300−500 °C and is probably associated with the dehydroxylation of the layers.[37] Meanwhile, the layer structure collapses, and LDH materials transform into the corresponding oxides.[28,38,39] Finally, the slight weight loss recorded above 500 °C is ascribed to the crystallization of new phases.[36] Thus, the thermal analysis indicates that thermally stable phases are formed at ∼550 °C (after the second weight loss and the collapse of layer structures). Furthermore, similar curves were observed when vanadium content increased to 0.5; however, the first weight-loss step shifts toward relatively lower temperature, and the weight loss decreases dramatically when the vanadium content further increases to 0.7 and 1. It suggests that $Mg_2Al_{0.3}V_{0.7}$−LDH, Mg_2V−LDH, and corresponding derived oxides possess remarkably different features compared with the other catalysts. In addition, the total weight loss decreases with an increase in the vanadium content, thus assigning the result to the oxidation process of V^{3+} to V^{5+}.[28,30]

The surface composition of $Mg_2Al_xV_{1-x}O$ catalysts was analyzed by the XPS method; the corresponding data are listed in Table 2. It can be seen clearly that it contains only O, V, Mg,

Table 2. Surface Elemental Composition of $Mg_2Al_xV_{1-x}O$ Catalysts Derived from XPS Analysis

sample	O 1s (at. %)	V 2p (at. %)	Al 2p (at. %)	Mg 2p (at. %)	S 2p (at. %)	V/(Al + V) molar ratio
$Mg_2Al_{0.9}V_{0.1}O$	66.75	1.44	9.56	22.25		0.13
$Mg_2Al_{0.7}V_{0.3}O$	69.09	3.21	6.87	20.83		0.32
$Mg_2Al_{0.5}V_{0.5}O$	68.91	4.54	4.79	21.76		0.49
$Mg_2Al_{0.3}V_{0.7}O$	73.00	5.42	2.90	18.65		0.65
Mg_2VO	72.21	8.16		19.25		1
$Mg_2Al_{0.7}V_{0.3}O$-used	66.06	3.56	7.05	21.86	1.47	0.33

and Al elements in all the fresh catalysts. It suggests that the parent LDH materials have been transformed into the corresponding oxides, which is consistent with TG results. The V/(V + Al) is in accordance with the EDS analysis.

Nitrogen adsorption−desorption isotherms and the BJH pore size distribution calculated from the desorption branch of all samples are displayed in Figure 3, and the textural properties are collected in Table 3. The catalysts exhibit type IV isotherms with clear hysteresis loops, a typical characteristic of mesoporous materials,[40] when the vanadium content is in the

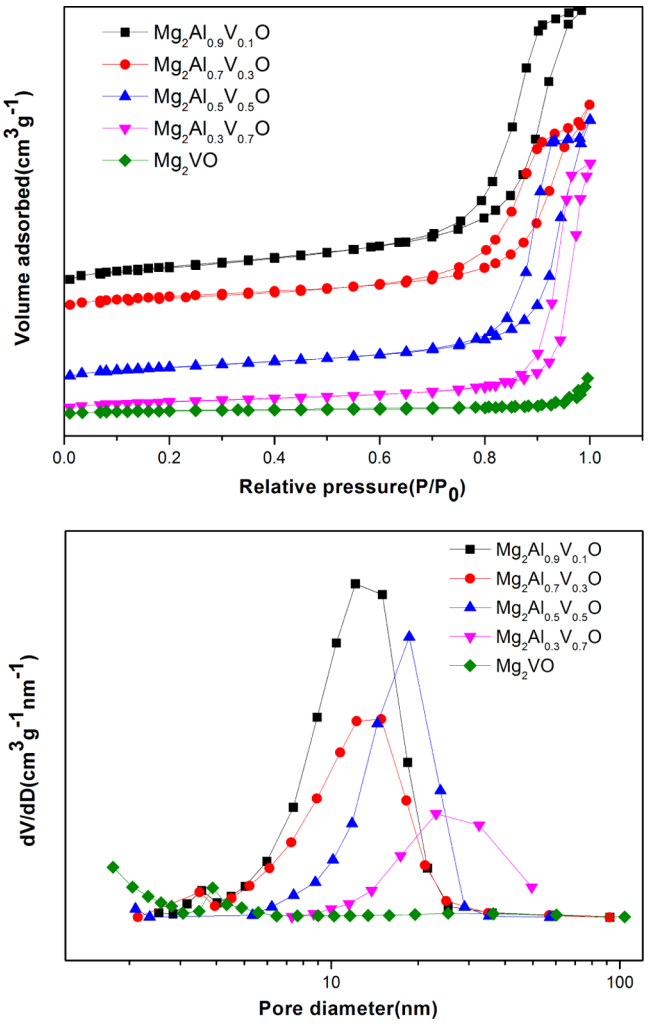

Figure 3. Nitrogen adsorption/desorption isotherms and pore size distribution calculated from the desorption branch of $Mg_2Al_xV_{1-x}O$ catalysts.

dx.doi.org/10.1021/cs500303y | ACS Catal. 2014, 4, 1500−1510

Table 3. Textural and Reducibility Properties of $Mg_2Al_xV_{1-x}O$ Catalysts

sample	S_{BET}[a] (m^2/g)	V_g[b] (cm^3/g)	D_p[c] (nm)	H_2 consumption (mmol $g^{-1}_{catalyst}$)
$Mg_2Al_{0.9}V_{0.1}O$	55	0.23	13	0.43
$Mg_2Al_{0.7}V_{0.3}O$	36	0.16	14	0.69
$Mg_2Al_{0.5}V_{0.5}O$	40	0.20	17	1.25
$Mg_2Al_{0.3}V_{0.7}O$	23	0.19	27	2.30
Mg_2VO	8	0.03	14	2.47

[a]BET specific surface area calculated at $P/P_0 = 0.05-0.25$. [b]Total pore volume estimated at $P/P_0 = 0.99$. [c]BJH pore diameter calculated from the desorption branch.

range of 0.1−0.7. Simultaneously, the step of hysteresis loops shifts toward relatively higher pressure with an increase in the vanadium content. It implies that the pore diameter increases with the addition of vanadium species,[41] which is in accordance with the pore size distribution. Moreover, when the vanadium content is increased to 1, the hysteresis loop becomes rather weak and the pore size distribution is nearly a straight line. It indicates that the pore structure has collapsed and a larger particle was formed.[40] It is consistent with the significant decrease in the BET surface area and SEM results.

3.2. The Chemical Status of Vanadium Species in $Mg_2Al_xV_{1-x}O$ Catalysts. The nature of the vanadium species presented on catalyst surface is important for determining the properties of catalyst as well as the catalytic performance. In this view, the V 2p XPS spectra of all samples are displayed in Figure 4. The O 1s signal is centered at ∼530 eV, and their satellites were subtracted to study the V 2p signal. The V 2p spectra are composed of V $2p_{3/2}$ and V $2p_{1/2}$ peaks due to the spin−orbit splitting, separated by 7−8 eV. In the case of fresh catalysts, the V $2p_{3/2}$ spectra present two peaks occurring at around 517 and 515.9 eV, corresponding to V^{5+} and V^{4+}, respectively. The XPS analysis reveals the coexistence of V^{5+} and V^{4+} species; the spectra are dominated by the peak attributed to V^{5+}. Thus, it suggests that vanadium species exist mainly in form of V^{5+} species; however, the cooperation environment for V^{5+} is still unclear.

Raman spectra of all samples are shown in Supporting Information Figure S2. The neat spectra reveal the presence of two bands at 830 and 863 nm as the main features of the catalysts. As reported, both bands correspond to the presence of crystalline $Mg_3V_2O_8$.[42] Therefore, it confirms the formation of $Mg_3V_2O_8$ in catalysts, which is in good agreement with the XRD results. Furthermore, the $Mg_3V_2O_8$ content first decreases with the vanadium content increase from 0.1 to 0.3, then it further increases with the vanadium content increase from 0.5 to 1, and the $Mg_3V_2O_8$ content increases in the order: $Mg_2Al_{0.7}V_{0.3}O$ < $Mg_2Al_{0.5}V_{0.5}O$ < $Mg_2Al_{0.9}V_{0.1}O$ < $Mg_2Al_{0.3}V_{0.7}O$ < Mg_2VO.

Further information on V^{5+} is provided by UV analysis. As shown in Figure 5, it can be clearly observed that all curves exhibit two main bands in the region of 200−600 nm. The band centered at 250 nm can be assigned to the charge transfer ($O^{2-} \rightarrow V^{5+}$) transitions of isolated tetrahedrally coordinated vanadium species, that is, $[VO_4]$,[43,44] and the bands occurring at 350 nm are related to the polymer vanadium species, that is, $Mg_3V_2O_8$ species. It indicates that V^{5+} species are presented mainly in the form of isolated $[VO_4]$ and $Mg_3V_2O_8$. Moreover, a new band appears in the region 600−800 nm for all catalysts, which suggests the existence of V^{4+}. It is in accordance with the XPS analysis result.

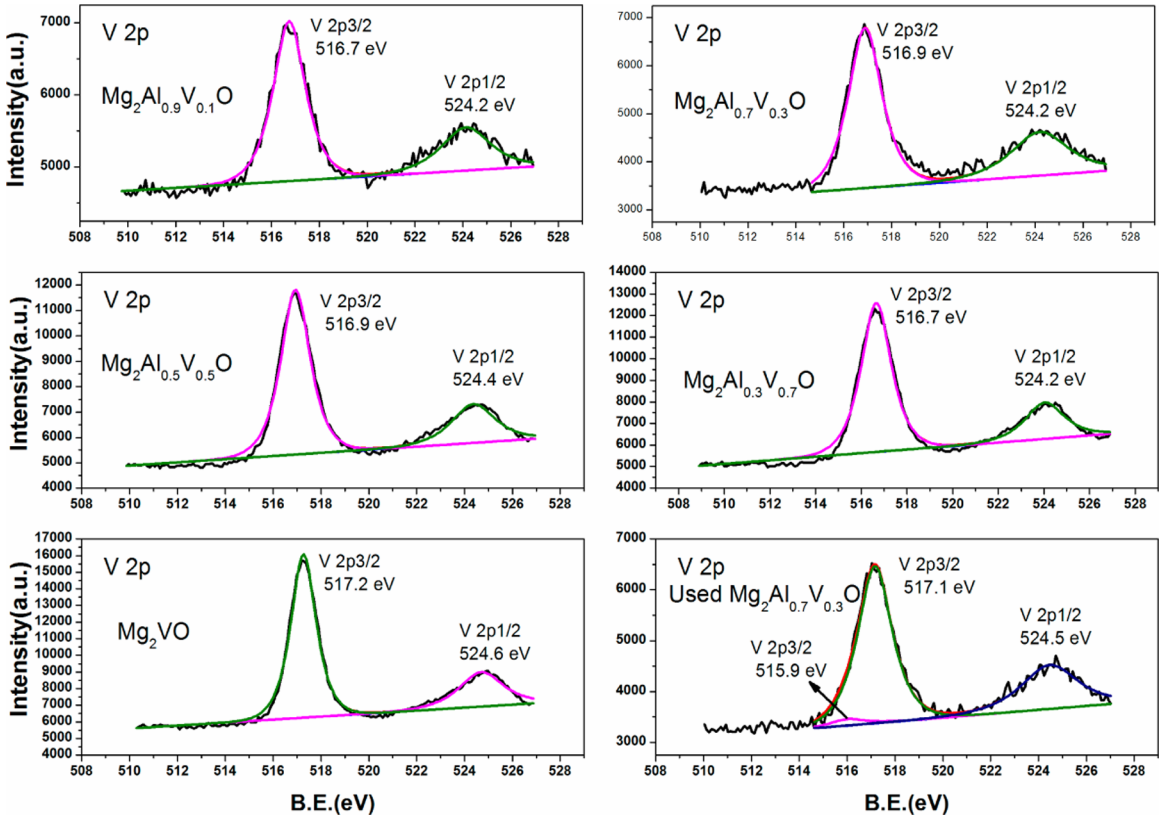

Figure 4. V 2p XPS spectra of $Mg_2Al_xV_{1-x}O$ catalysts.

dx.doi.org/10.1021/cs500303y | ACS Catal. 2014, 4, 1500−1510

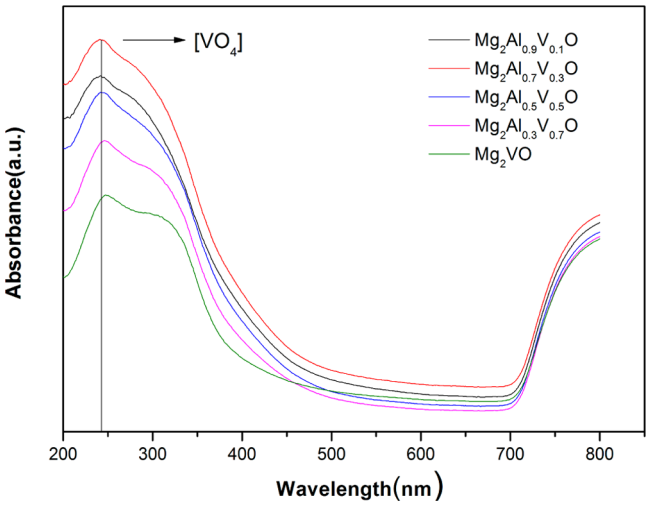

Figure 5. UV−vis DRS spectra of $Mg_2Al_xV_{1-x}O$ catalysts.

EPR is very sensitive to the ligand geometry of paramagnetic transition metal ions, and the signature of tetrahedrally coordinated V^{4+} significantly differs from that of the octahedrally coordinated ones. Thus, EPR was applied to further explore the cooperation environment of V^{4+} species in these catalysts. The EPR patterns of a representative catalyst ($Mg_2Al_{0.7}V_{0.3}O$) are illustrated in Figure 6. According to a

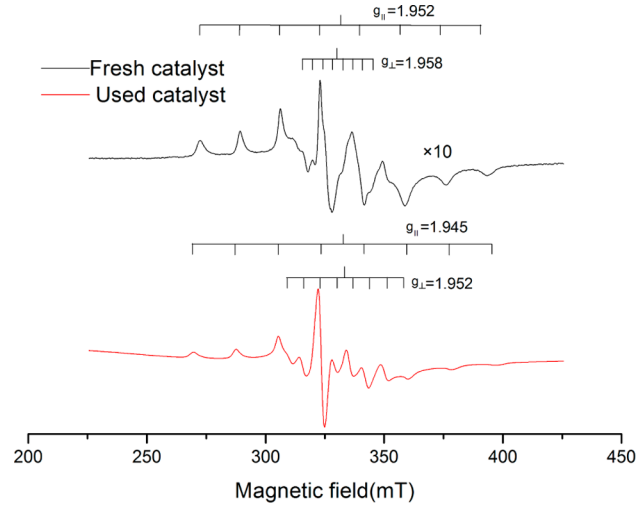

Figure 6. EPR spectra of $Mg_2Al_{0.7}V_{0.3}O$ catalyst.

previous report,[44] the values $g_{\|}$ = 1.952 and $g_{\perp}$ = 1.958 for fresh catalyst implies the presence of axially distorted VO^{2+} ions in octahedral coordination. Therefore, it can be concluded that some VO^{2+} ions are incorporated into the octahedral MgO structure and occupy the vacant Mg lattice position by substituting for Mg and cause damage to the MgO structure.

3.3. The Reductive Properties of $Mg_2Al_xV_{1-x}O$ Catalysts. The TPR profiles of all catalysts are established in Figure 7. In addition, a quantitative analysis on H_2 consumption calculated by integrating the H_2-TPR curves is collected in Table 3. As shown in Figure 7, all curves can be divided into two reduction peaks. The first peak occurring at a relatively lower temperature is attributed to the reduction of surface V^{5+} species in distorted [VO_4] species, although the peak occurring at a relatively higher temperature is related to the reduction of bulk V^{5+} species, which belongs to the bulk structure of Mg orthovanadate ($Mg_3V_2O_8$).[43,45] It is worth noting that the peak shifts toward relatively higher temperature with the rise of vanadium content from 0.3 to 1 (590 and 632 °C for $Mg_2Al_{0.7}V_{0.3}O$, 618 and 664 °C for $Mg_2Al_{0.5}V_{0.5}O$, 621 and 680 °C for $Mg_2Al_{0.3}V_{0.7}O$, 687 and 780 °C for Mg_2VO). This phenomenon indicates that a lower vanadium content is favorable for the redox of these catalysts.

3.4. The Basic Properties of $Mg_2Al_xV_{1-x}O$ Catalysts. The surface basicity of all catalysts was assessed by CO_2-TPD, and all profiles are depicted in Figure 8. For Mg_2AlO, the curve is characteristic, with three desorption peaks occurring at 100 °C (weak basic sites), 400 °C (moderate basic sites) and 600 °C (strong basic sites), respectively. As is known, the weak basic sites can be assigned to OH groups, the moderate basic sites are ascribed to the Mg−O bandm and the strong basic sites are associated with coordinatively unsaturated O^{2-} ions.[40] In particular, the curve is dominated by strong basic sites. Nevertheless, very different curves are obtained after vanadium modification. The moderate basicity is remarkably strengthened for $Mg_2Al_{0.9}V_{0.1}O$, $Mg_2Al_{0.7}V_{0.3}O$, and $Mg_2Al_{0.5}V_{0.5}O$ catalysts, caused by the abundant existence of MgO in these catalysts. Simultaneously, the strong basic sites nearly disappear for all catalysts, whereas the moderate basicity decreases with a rise in the vanadium content from 0.5 to 1 as a result of the gradual increase in the $Mg_3V_2O_8$ content and decrease in the MgO content. In addition, the moderate basicity decreases in the order $Mg_2Al_{0.7}V_{0.3}O$ > $Mg_2Al_{0.5}V_{0.5}O$ > $Mg_2Al_{0.9}V_{0.1}O$ > $Mg_2Al_{0.3}V_{0.7}O$ > Mg_2VO, which is consistent with the Raman and UV results. Among them, $Mg_2Al_{0.7}V_{0.3}O$ catalyst possesses the largest amount of moderate basic sites. Noticeably, the basic sites have disappeared in the Mg_2VO catalyst. This can be attributed to the collapse of the pore structure and most of Mg existing in the form of $Mg_3V_2O_8$.

4. CATALYTIC PERFORMANCES

4.1. Effect of Reaction Temperature. Figure 9A exhibits the effect of temperature on the catalytic activities of $Mg_2Al_xV_{1-x}O$ catalysts for H_2S selective oxidation. It can be observed that H_2S conversion initially increases with an increase in the reaction temperature to 180 °C, and then it remains almost constant when the temperature further increases to 200 °C. Nevertheless, the catalysts present an obviously different variation trend on H_2S conversion before and after 160 °C with an increase in the vanadium content. At less than 160 °C, the H_2S conversion increases with an increase in the vanadium content; however, the variation trend is extraordinarily consistent with that of moderate basic sites on the catalyst surface when the temperature exceeds 160 °C, that is, the H_2S conversion over theses catalysts decreases in the order $Mg_2Al_{0.7}V_{0.3}O$ > $Mg_2Al_{0.5}V_{0.5}O$ > $Mg_2Al_{0.9}V_{0.1}O$ > $Mg_2Al_{0.3}V_{0.7}O$ > Mg_2VO. The maximum H_2S conversion is obtained at 180 °C (nearly 100%) for the $Mg_2Al_{0.7}V_{0.3}O$ catalyst. Furthermore, the Mg_2VO catalyst exhibits particularly poor H_2S conversion compared with the other catalysts, which perhaps is due to the collapse of the pore structure and absence of moderate basic sites.

Figure 9B shows the relationship between sulfur selectivity and reaction temperature. It can be clearly found that the sulfur selectivity for all catalysts remains constant at 100% when the temperature is below 160 °C; however, the sulfur selectivity decreases with an increase in the temperature when the temperature exceeds 160 °C, and the variation trend with an

dx.doi.org/10.1021/cs500303y | ACS Catal. 2014, 4, 1500−1510

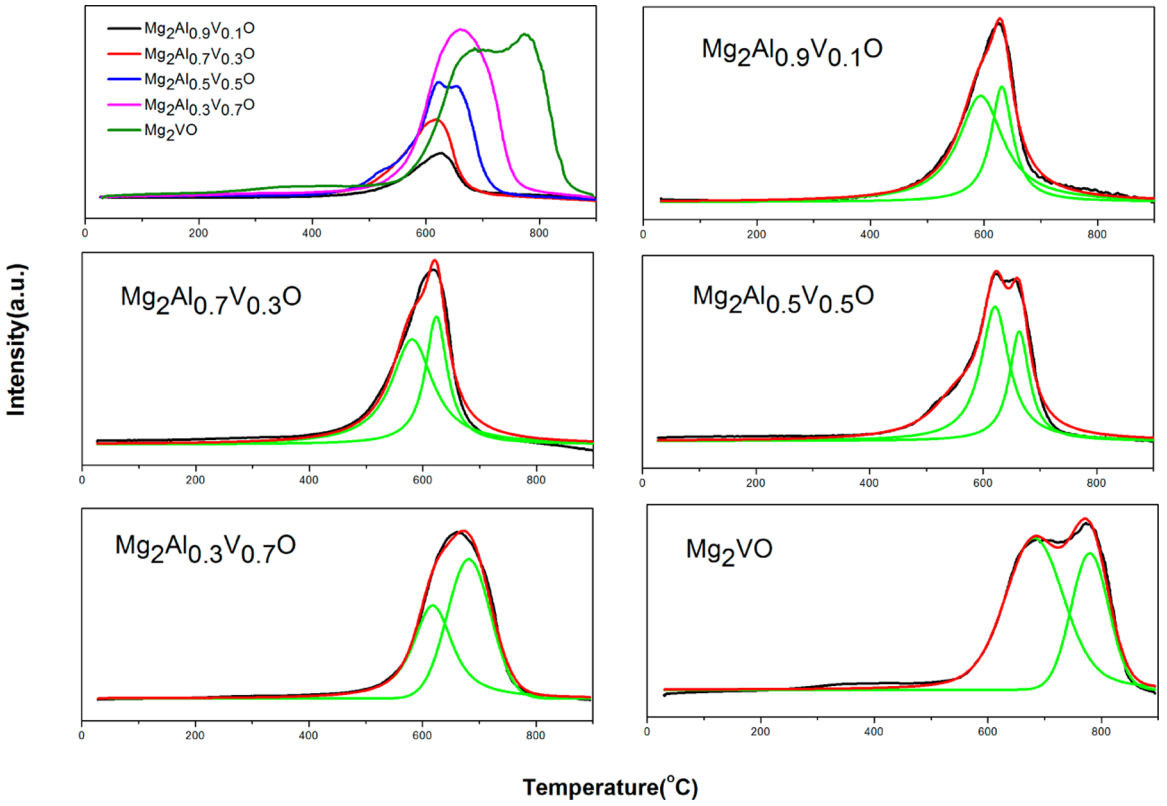

Figure 7. H_2-TPR spectra of the $Mg_2Al_xV_{1-x}O$ catalysts.

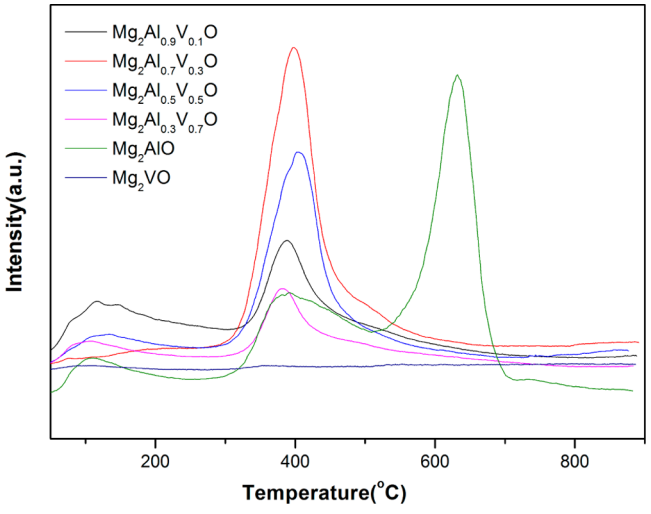

Figure 8. CO_2-TPD spectra of the $Mg_2Al_xV_{1-x}O$ catalysts.

increase in the vanadium content is extraordinarily opposite that of moderate basic sites on the catalyst surface, that is, the sulfur selectivity over these catalysts increases in the order $Mg_2Al_{0.7}V_{0.3}O$ < $Mg_2Al_{0.5}V_{0.5}O$ < $Mg_2Al_{0.9}V_{0.1}O$ < $Mg_2Al_{0.3}V_{0.7}O$ < Mg_2VO. Nevertheless, the sulfur selectivity is still higher than 90% for all catalysts. Thus, the catalysts exhibit excellent sulfur selectivity.

Meanwhile, the relationship between sulfur yield and reaction temperature is shown in Figure 9C. Apparently, the variation trend is similar to that of H_2S conversion when the temperature is below 160 °C, because of the high sulfur selectivity (100%). However, the sulfur yield changes slightly when the temperature increases to 200 °C, which is attributed to the opposite variation trend of the sulfur selectivity compared with H_2S conversion. Likewise, the maximum sulfur yield (95%) is obtained at 180 °C for the $Mg_2Al_{0.7}V_{0.3}O$ catalyst. Therefore, compared with the other metal oxide catalysts,[4,5,7,46,47] the reaction temperature is decreased efficiently and the catalytic activities are improved significantly. Moreover, the Mg_2VO catalyst exhibits particularly low catalytic activity due to the poor H_2S conversion.

4.2. Durability of $Mg_2Al_xV_{1-x}O$ Catalysts. Figure 10 shows the durability behavior of $Mg_2Al_{0.7}V_{0.3}O$ catalyst at 180 °C with a reactant composition of $H_2S/O_2/N_2$ = 5/2.5/92.5 at GHSV = 24 000 h^{-1}. It can be observed clearly that the H_2S conversion, sulfur selectivity, and sulfur yield are all >90% after 20 h of reaction. Thus, the $Mg_2Al_{0.7}V_{0.3}O$ catalyst exhibits reasonable durability under these conditions. Moreover, it can be seen that at the initial stage of the reaction, H_2S conversion and sulfur yield are 99% and 95%, respectively, whereas both of them decreased to 91% as time proceeded. Conversely, the sulfur selectivity increased from 96% to 100%.

4.3. Catalytic Reaction and Deactivation Mechanisms. The catalytic performances reveal that the catalysts present remarkably different variation trends with an increase in the vanadium content before and after 160 °C. The variation trend of the H_2S conversion with the increase in vanadium content is opposite that of the sulfur selectivity when the temperature exceeds 160 °C. Obviously, both the H_2S conversion and sulfur selectivity are particularly influenced by the basicity of the catalyst. Moreover, the Mg_2VO catalyst exhibits rather poor catalytic activity, which can be associated with the absence of basic sites. Therefore, it is important to clarify the catalytic reaction mechanism and investigate the role of basic sites in the H_2S selective oxidation process. Herein, the DRIFTS-MS

dx.doi.org/10.1021/cs500303y | ACS Catal. 2014, 4, 1500−1510

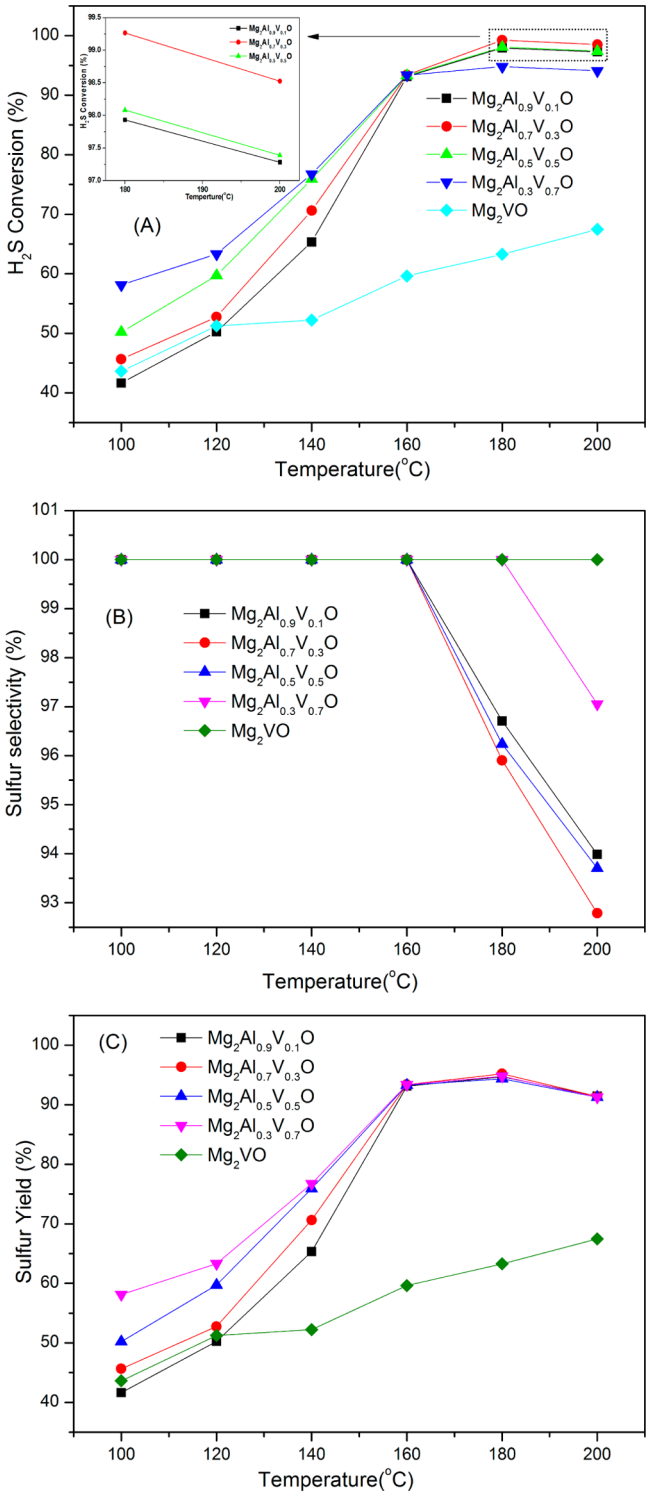

Figure 9. Effect of temperature on (A) conversion of H_2S, (B) sulfur selectivity, and (C) sulfur yield for $Mg_2Al_xV_{1-x}O$ catalysts.

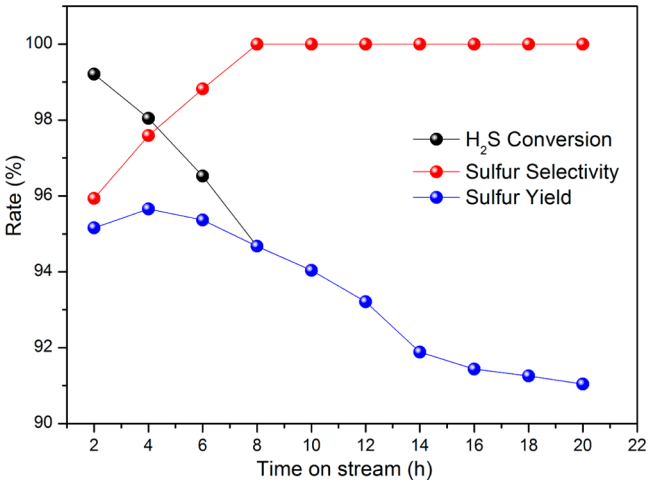

Figure 10. Time-on-stream behavior of $Mg_2Al_{0.7}V_{0.3}O$ catalyst for H_2S selective oxidation at 180 °C.

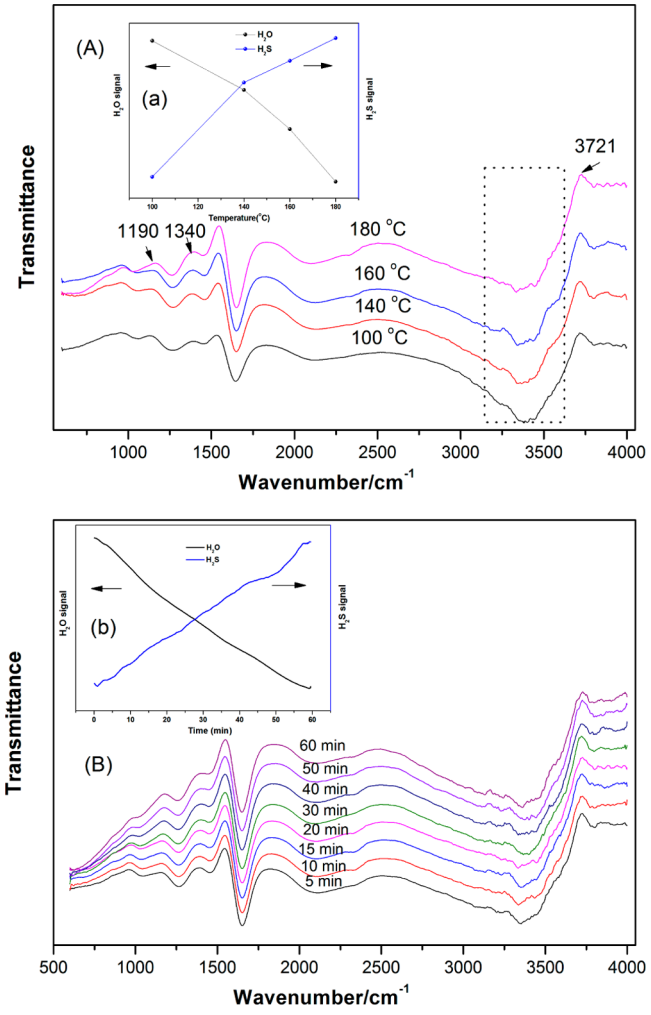

Figure 11. DRIFTS-MS spectra of $Mg_2Al_{0.7}V_{0.3}O$ treated with a flow of 5000 ppm of H_2S at (A) different temperatures and (B) various times at 180 °C.

approach was applied to explore the catalytic mechanism and the role of basic sites.

Figure 11 shows the H_2S adsorbed DRIFTS-MS spectra (5000 ppm of H_2S in 200 mL/min flow) of $Mg_2Al_{0.7}V_{0.3}O$ catalyst at various reaction temperatures and times. It is known that H_2S can be adsorbed onto a catalyst's surface through four routes:[48,49] (1) It can dissociatively adsorb onto the catalyst's surface to form an HS− (2577 cm^{-1}) and a hydroxyl group (3500 cm^{-1}). (2) It can react with surface hydroxyl groups (a negative band appeared at 3700 cm^{-1}) to form HS− (2577 cm^{-1}) and molecularly adsorbed H_2O (1633 and 3500 cm^{-1}). (3) It can adsorb onto a surface defective site, causing

dx.doi.org/10.1021/cs500303y | ACS Catal. 2014, 4, 1500−1510

incorporation of S^{2-} in the lattice. It includes the consumption of a hydroxyl group (a negative band appeared at 3700 cm^{-1}) and the formation of adsorbed H_2O as well as a new hydroxyl group (1630 and 3500 cm^{-1}, respectively). (4) The high surface basicity makes it probable that S^{2-} can be incorporated directly into the surface and form H_2O.

As shown in Figure 11a (the MS signal value at each specific temperature point is the average value in 20 min) and b, the H_2S MS signal increased with an increase in the temperature and as time proceeded. It indicates that H_2S can be adsorbed onto the catalyst surface. However, in Figure 11A and B, no new bands are observed in the regions attributed to HS− (2577 cm^{-1}), adsorbed H_2O, and new hydroxyl group (1633, 3500 cm^{-1}). Simultaneously, no consumption of hydroxyl groups (negative band at 3700 cm^{-1}) is detected for all H_2S adsorbed spectra. It indicates that H_2S cannot be adsorbed onto the catalyst's surface through the first three routes. Furthermore, the band at 1340 cm^{-1} coincides with physisorbed SO_2,[49,50] which results from the interaction of S^{2-} with the lattice oxygen. Thus, it shows the existence of S^{2-} in the adsorption process. Meanwhile, it is important to observe that a H_2O MS signal appears and changes in the adsorption process (Figure 11a,b). It means that H_2O was formed during the H_2S adsorption process, but the formed H_2O cannot be adsorbed on the catalyst surface. Thus, it can be tentatively deduced that the H_2S can be adsorbed onto the catalyst surface via route 4,[49] that is, H_2S can be adsorbed onto the moderate basic sites of catalysts.

It is known that vanadium-based catalysts obey a stepwise mechanism in H_2S selective oxidation reaction, that is, V^{5+} was first reduced by H_2S to form S_n and V^{4+}, and then V^{4+} was oxidized to V^{5+} by oxygen in a separate step. In addition, one should also take into account that the catalysts present rather poor catalytic activity when the basic sites are no longer there. Thus, it seems probable that H_2S was first adsorbed onto the moderate basic sites of the catalyst, and then it was oxidized to S_n by vanadium species. Herein, a catalytic reaction mechanism over the $Mg_2Al_xV_{1-x}O$ catalysts can be tentatively proposed as the following:

$$Mg - O - Mg + H_2S \rightarrow Mg - S - Mg + H_2O \quad (8)$$

$$Mg - S - Mg + V^{5+} \rightarrow Mg{-}{-}Mg + V^{4+} + S_n \quad (9)$$

$$V^{4+} + Mg{-}{-}Mg + (1/2)O_2 \rightarrow Mg - O - Mg + V^{5+} \quad (10)$$

In a typical reaction process, H_2S is first adsorbed onto the Mg−O band of MgO (moderate basic site), forming S^{2-} and H_2O. Then the S^{2-} is oxidized to S_n by V^{5+}, forming oxygen vacancies in the process. Finally, V^{4+} is oxidized to V^{5+} by O_2, and O^{2-} is incorporated into oxygen vacancies of the Mg−O band. Therefore, the H_2S adsorption ability of the catalyst is extraordinarily consistent with the variation trend of moderate basic sites on the catalyst surface, that is, the H_2S adsorption ability of the catalyst decreases in the order $Mg_2Al_{0.7}V_{0.3}O$ > $Mg_2Al_{0.5}V_{0.5}O$ > $Mg_2Al_{0.9}V_{0.1}O$ > $Mg_2Al_{0.3}V_{0.7}O$ > Mg_2VO.

The catalytic performances can be reasonably explained by this catalytic reaction mechanism. As shown in Figure 11a,b the H_2O MS signal decreases and H_2S MS signal increases with an increase in the temperature and as time proceeds, implying that the H_2S adsorption ability decreases with an increase in the temperature. Therefore, H_2S can be adsorbed onto the catalyst's surface strongly and abundantly at a relatively lower temperature, and the H_2S conversion depends mainly on the activity and quantity of V^{5+}; that is, the activity and quantity of V^{5+} is the rate-determining step. Hence, the conversion increases with an increase in the vanadium content. Moreover, the V^{5+} becomes more active with the increase in the temperature, which results in the increase in the conversion. However, the catalytic activity of V^{5+} is improved significantly and H_2S adsorption ability seems rather weak when the temperature exceeds 160 °C; thus, H_2S adsorption ability instead of V^{5+} becomes the rate-determining step for H_2S conversion. Therefore, the H_2S conversion variation trend is extraordinarily consistent with that of moderate basic sites on the catalyst surface when the temperature exceeds 160 °C. The enhanced reducibility of $Mg_2Al_{0.9}V_{0.1}O$ and $Mg_2Al_{0.7}V_{0.3}O$ catalysts is also beneficial to the reaction. On the other hand, the variation trend of the sulfur selectivity can be explained by the fact that SO_2 can be formed above the sulfur dew-point temperature (180 °C); thus, a higher conversion leads to more formation of SO_2 in the presence of O_2, that is, a lower sulfur selectivity.

To explore the catalyst deactivation mechanism, the V 2p and S 2p XPS spectrum of used $Mg_2Al_{0.7}V_{0.3}O$ catalyst are provided in Figures 4 and 12. For the S 2p spectrum, it is fitted

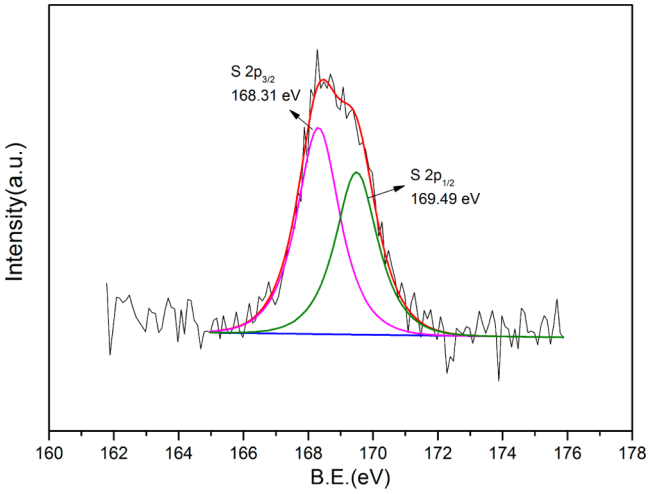

Figure 12. S 2p XPS spectra of the used $Mg_2Al_{0.7}V_{0.3}O$ catalyst.

with one spin−orbit doublet situated at binding energies of 168.31 and 169.54 eV for the S $2p_{3/2}$ and S $2p_{1/2}$ peaks, respectively. Both the S $2p_{3/2}$ and S $2p_{1/2}$ peaks are related to the presence of the SO_4^{2-} species.[51] It is also confirmed by the FTIR analysis of the used catalyst (Supporting Information Figure S3), as a new peak appears at 1190 cm^{-1}, which is also assigned to the SO_4^{2-} species. In addition, in H_2S adsorbed DRIFT spectra (Figure 11A,B), the band appearing at 1190 cm^{-1} is also attributed to SO_4^{2-} species. Moreover, for the V 2p spectrum of the used catalyst, the asymmetry V $2p_{3/2}$ peak can also be divided into two peaks at 515.9 and 517.1 eV that are attributed to V^{4+} and to V^{5+}, respectively. However, the area percentage of V^{4+} increased from 2.5% to 8% compared with fresh catalyst. Hence, it indicates that more V^{4+} species was formed after the reaction. In addition, the sulfur content detected by XPS is 2.4 wt %. The above information indicates the formation of less active $VOSO_4$ with low content. Simultaneously, the EPR spectrum of the used catalyst is presented in Figure 6, and the values of $g_{\|}$ and $g_{\perp}$ for used

dx.doi.org/10.1021/cs500303y | ACS Catal. 2014, 4, 1500−1510

catalyst remain almost consistent with the fresh catalyst. However, the peak intensity is strengthened significantly for the used catalyst (10 times that of the fresh catalyst), indicating that more VO^{2+} was formed in the reaction. It is in good agreement with the XPS analysis. The Raman and XRD spectrum of used catalyst are also presented in Supporting Information Figures S4 and S5, respectively. It is very important to observe that more $Mg_3V_2O_8$ was formed and the content of MgO was decreased sharply after the reaction. Thus, the catalyst deactivation mechanism can be tentatively proposed as the following: In the reaction, the newly formed VO^{2+} can occupy octahedral Mg lattice positions, leading to damage of the MgO structure. It associates with the increase of $Mg_3V_2O_8$ content, which results in a decrease in the MgO content, that is, moderate basic sites. Herein, the H_2S cannot adsorb onto the basic sites efficiently, causing a decrease in the catalytic performance and catalyst deactivation. Moreover, the formed less-active $VOSO_4$ also contributes to the catalyst deactivation.

5. CONCLUSIONS

A series of $Mg_2Al_xV_{1-x}$−LDH were synthesized by using a facile method, and the derived oxides were tested for H_2S selective oxidation. It was observed that vanadium species mainly existed in the form of isolated V^{5+} in distorted $[VO_4]$, $Mg_3V_2O_8$, and VO^{2+}. Significantly, the catalysts exhibit a high catalytic activity at a relatively lower reaction temperature range (100−200 °C) as a result of the well-dispersed vanadium species and excellent moderate basicity property, which is beneficial because of the abundance of MgO. The catalytic reaction mechanism over these catalysts was proposed as follows: H_2S is first adsorbed onto the Mg−O−Mg band of MgO (moderate basic sites), forming S^{2-} and H_2O. Then, the S^{2-} is oxidized to S_n by V^{5+}, forming oxygen vacancies in the process. Finally, V^{4+} is oxidized to V^{5+} by O_2, and O^{2-} is incorporated into the oxygen vacancies. In addition, the catalyst deactivation is due mainly to the decrease in the moderate basic sites. Moreover, the formed less-active $VOSO_4$ also contributes to the catalyst deactivation.

■ ASSOCIATED CONTENT

Supporting Information

Additional information as noted in text. This material is available free of charge via the Internet at http://pubs.acs.org.

■ AUTHOR INFORMATION

Corresponding Author

*Phone: +86-10-62923564. Fax: +86-10-62923564. E-mail: zpinghao@rcees.ac.cn.

Notes

The authors declare no competing financial interest.

■ ACKNOWLEDGMENTS

This work was financially supported by the National High Technology Research and Development Program of China (No. 2012AA063101); the National Basic Research Program of China (No. 2010CB732300); the National Natural Science Foundation (21337003); and the Science Promotion Program of Research Center for Eco-Environmental Sciences, CAS (YSW2013B05).

■ REFERENCES

(1) Shinkarev, V. V.; Glushenkov, A. M.; Kuvshinov, D. G.; Kuvshinov, G. G. *Carbon* **2010**, *48*, 2004−2012.
(2) Zhang, X.; Dou, G. Y.; Wang, Z.; Li, L.; Wang, Y. F.; Wang, H. L.; Hao, Z. P. *J. Hazard. Mater.* **2013**, *260*, 104−111.
(3) Zhang, X.; Dou, G. Y.; Wang, Z.; Cheng, J.; Wang, H. L.; Ma, C. Y.; Hao, Z. P. *Catal. Sci. Technol.* **2013**, *3*, 2778−2785.
(4) Bineesh, K. V.; Kim, D. K.; Kim, M. I.; Selvaraj, M.; Park, D. W. *Dalton Trans.* **2011**, *40*, 3938−3945.
(5) Bineesh, K. V.; Kim, D. K.; Kim, M. I. L.; Park, D. W. *Appl. Clay Sci.* **2011**, *53*, 204−211.
(6) Shin, M. Y.; Park, D. W.; Chung, J. S. *Appl. Catal., B* **2001**, *30*, 409−419.
(7) Bineesh, K. V.; Kim, D. K.; Kim, D. W.; Cho, H. J.; Park, D. W. *Energy Environ. Sci.* **2010**, *3*, 302−310.
(8) Reyes-Carmona, Á.; Soriano, M. D.; López Nieto, J. M.; Jones, D. J.; Jiménez-Jiménez, J.; Jiménez-López, A.; Rodríguez-Castellón, E. *Catal. Today* **2013**, *210*, 117−123.
(9) Soriano, M. D.; Jimenez-Jimenez, J.; Concepcion, P.; Jimenez-Lopez, A.; Rodriguez-Castellon, E.; Nieto, J. M. L. *Appl.Catal., B* **2009**, *92*, 271−279.
(10) Eggenhuisen, T. M.; van Steenbergen, M. J.; Talsma, H.; de Jongh, P. E.; de Jong, K. P. *J. Phys. Chem. C* **2009**, *113*, 16785−16791.
(11) Espinosa-Alonso, L.; O'Brien, M. G.; Jacques, S. D. M.; Beale, A. M.; de Jong, K. P.; Barnes, P.; Weckhuysen, B. M. *J. Am. Chem. Soc.* **2009**, *131*, 16932−16938.
(12) Neimark, A. V.; Kheifets, L. I.; Fenelonov, V. B. *Ind. Eng. Chem. Prod. Res. Dev.* **1981**, *20*, 439−450.
(13) Xu, Z. P.; Zhang, J.; Adebajo, M. O.; Zhang, H.; Zhou, C. H. *Appl. Clay Sci.* **2011**, *53*, 139−150.
(14) Karásková, K.; Obalová, L.; Jirátová, K.; Kovanda, F. *Chem. Eng. J.* **2010**, *160*, 480−487.
(15) Wang, S. H.; Wang, Y. B.; Dai, Y.-M.; Jehng, J. M. *Appl. Catal., A* **2012**, *439*−*440*, 135−141.
(16) Zhou, C. H. *Appl. Clay Sci.* **2011**, *53*, 87−96.
(17) Caravaggio, G. A.; Detellier, C.; Wronski, Z. *J. Mater. Chem.* **2001**, *11*, 912−921.
(18) Xu, Z. P.; Stevenson, G.; Lu, C. Q.; Lu, G. Q. *J. Phys. Chem. B* **2006**, *110*, 16923−16929.
(19) Carja, G.; Nakamura, R.; Aida, T.; Niiyama, H. *J. Catal.* **2003**, *218*, 104−110.
(20) Pausch, I.; Lohse, H. H.; Schurmann, K.; Allmann, R. *Clays Clay Miner.* **1986**, *34*, 507−510.
(21) Yu, J. J.; Jiang, Z.; Zhu, L.; Hao, Z. P.; Xu, Z. P. *J. Phys. Chem. B* **2006**, *110*, 4291−4300.
(22) Buchheit, R. G.; Guan, H.; Mahajanam, S.; Wong, F. *Prog. Org. Coat.* **2003**, *47*, 174−182.
(23) Zheludkevich, M. L.; Poznyak, S. K.; Rodrigues, L. M.; Raps, D.; Hack, T.; Dick, L. F.; Nunes, T.; Ferreira, M. G. S. *Corros. Sci.* **2010**, *52*, 602−611.
(24) Barriga, C.; Jones, W.; Malet, P.; Rives, V.; Ulibarri, M. A. *Inorg. Chem.* **1998**, *37*, 1812−1820.
(25) Mahajanam, S. P. V.; Buchheit, R. G. *Corrosion* **2008**, *64*, 230−240.
(26) Salak, A. N.; Tedim, J.; Kuznetsova, A. I.; Ribeiro, J. L.; Vieira, L. G.; Zheludkevich, M. L.; Ferreira, M. G. S. *Chem. Phys.* **2012**, *397*, 102−108.
(27) Salak, A. N.; Tedim, J.; Kuznetsova, A. I.; Zheludkevich, M. L.; Ferreira, M. G. S. *Chem. Phys. Lett.* **2010**, *495*, 73−76.
(28) Labajos, F. M.; Sastre, M. D.; Trujillano, R.; Rives, V. *J. Mater. Chem.* **1999**, *9*, 1033−1039.
(29) Kuśtrowski, P.; Sułkowska, D.; Chmielarz, L.; Rafalska-Łasocha, A.; Dudek, B.; Dziembaj, R. *Microporous Mesoporous Mater.* **2005**, *78*, 11−22.
(30) Shannon, R. D. *Acta Crystallogr., Sect. A* **1976**, *32*, 751−767.
(31) Velu, S.; Shah, N.; Jyothi, T. M.; Sivasanker, S. *Microporous Mesoporous Mater.* **1999**, *33*, 61−75.
(32) Dula, R.; Wcislo, K.; Stoch, J.; Grzybowska, B.; Serwicka, E. M.; Kooli, F.; Bahranowski, K.; Gawel, A. *Appl. Catal., A* **2002**, *230*, 281−291.
(33) Blanco, S.; Carrazán, S. R. G.; Rives, V. *Appl. Catal., A* **2008**, *342*, 93−98.

(34) Bahranowski, K.; Bueno, G.; Cortés Corberán, V.; Kooli, F.; Serwicka, E. M.; Valenzuela, R. X.; Wcisło, K. *Appl. Catal., A* **1999**, *185*, 65−73.
(35) Li, P.; He, C.; Cheng, J.; Ma, C. Y.; Dou, B. J.; Hao, Z. P. *Appl. Catal., B* **2011**, *101*, 570−579.
(36) Holgado, M. J.; Labajos, F. M.; Montero, M. J. S.; Rives, V. *Mater. Res. Bull.* **2003**, *38*, 1879−1891.
(37) Qi, F.; Zhang, X.; Li, S. *J. Phys. Chem. Solids* **2013**, *74*, 1101−1108.
(38) Xu, Z. P.; Zeng, H. C. *J. Phys. Chem. B* **2000**, *104*, 10206−10214.
(39) Bera, P.; Rajamathi, M.; Hegde, M. S.; Kamath, P. V. *Bull. Mater. Sci.* **2000**, *23*, 141−145.
(40) Wu, G.; Wang, X.; Wei, W.; Sun, Y. *Appl. Catal., A* **2010**, *377*, 107−113.
(41) Xia, S.; Nie, R.; Lu, X.; Wang, L.; Chen, P.; Hou, Z. *J. Catal.* **2012**, *296*, 1−11.
(42) López Nieto, J. M.; Dejoz, A.; Vazquez, M. I.; O'Leary, W.; Cunningham, J. *Catal. Today* **1998**, *40*, 215−228.
(43) Dias, A. P. S.; Dimitrov, L. D.; Oliveira, M. C. R.; Zavoianu, R.; Fernandes, A.; Portela, M. F. *J. Non-Cryst. Solids* **2010**, *356*, 1488−1497.
(44) Rybarczyk, P.; Berndt, H.; Radnik, J.; Pohl, M. M.; Buyevskaya, O.; Baerns, M.; Brückner, A. *J. Catal.* **2001**, *202*, 45−58.
(45) Balderas-Tapia, L.; Wang, J. A.; Hernández-Pérez, I.; Aguilar-Ríos, G. G.; Schacht, P. *Mater. Lett.* **2004**, *58*, 3034−3039.
(46) Lavalley, J.-C.; Travert, J.; Chevreau, T.; Lamotte, J.; Saur, O. *J. Chem. Soc., Chem. Commun.* **1979**, 146−148.
(47) Toops, T. J.; Crocker, M. *Appl. Catal., B* **2008**, *82*, 199−207.
(48) Koyuncu, D. D. E.; Yasyerli, S. *Ind. Eng. Chem. Res.* **2009**, *48*, 5223−5229.
(49) Yasyerli, S.; Dogu, G.; Dogu, T. *Catal. Today* **2006**, *117*, 271−278.
(50) Xu, W.; He, H.; Yu, Y. *J. Phys. Chem. C* **2009**, *113*, 4426−4432.
(51) Cantrell, K. J.; Yabusaki, S. B.; Engelhard, M. H.; Mitroshkov, A. V.; Thornton, E. C. *Environ. Sci. Technol.* **2003**, *37*, 2192−2199.